



Derivation and compilation of lower-atmospheric properties relating to temperature, wind, stability, moisture, and surface radiation budget over the central Arctic sea ice during MOSAiC

Gina C. Jozef^{1,2,3}, Robert Klingel⁴, John J. Cassano^{1,2,3}, Björn Maronga^{4,5}, Gijs de Boer^{2,6,7}, Sandro Dahlke⁸, and Christopher J. Cox⁶

¹Dept. of Atmospheric and Oceanic Sciences, University of Colorado Boulder, Boulder, CO, USA

²Cooperative Institute for Research in Environmental Sciences,
University of Colorado Boulder, Boulder, CO, USA

³National Snow and Ice Data Center, University of Colorado Boulder, Boulder, CO, USA

⁴Leibniz University Hanover, Institute of Meteorology and Climatology, Hanover, Germany

⁵Geophysical Institute, University of Bergen, Bergen, Norway

⁶NOAA Physical Sciences Laboratory, Boulder, CO, USA

⁷Integrated Remote and In Situ Sensing, University of Colorado Boulder, Boulder, CO, USA

⁸Alfred Wegener Institute Helmholtz Centre for Polar and Marine Research, Potsdam, Germany

Correspondence: Gina C. Jozef (gina.jozef@colorado.edu)

Received: 11 April 2023 – Discussion started: 4 July 2023

Revised: 29 September 2023 – Accepted: 4 October 2023 – Published: 10 November 2023

Abstract. Atmospheric measurements taken over the span of an entire year between October 2019 and September 2020 during the icebreaker-based Multidisciplinary drifting Observatory for the Study of Arctic Climate (MOSAiC) expedition provide insight into processes acting in the Arctic atmosphere. Through the merging of disparate yet complementary in situ observations, we can derive information about these thermodynamic and kinematic processes with great detail. This paper describes methods used to create a lower-atmospheric properties dataset containing information on several key features relating to the central Arctic atmospheric boundary layer, including properties of temperature inversions, low-level jets, near-surface meteorological conditions, cloud cover, and the surface radiation budget. The lower-atmospheric properties dataset was developed using observations from radiosondes launched at least four times per day, a 10 m meteorological tower and radiation station deployed on the sea ice near the research vessel *Polarstern*, and a ceilometer located on the deck of the *Polarstern*. This lower-atmospheric properties dataset, which can be found at <https://doi.org/10.1594/PANGAEA.957760> (Jozef et al., 2023), contains metrics which fall into the overarching categories of temperature, wind, stability, clouds, and radiation at the time of each radiosonde launch. The purpose of the lower-atmospheric properties dataset is to provide a consistent description of general atmospheric boundary layer conditions throughout the MOSAiC year, which can aid in research applications with the overall goal of gaining a greater understanding of the atmospheric processes governing the central Arctic and how they may contribute to future climate change.

1 Introduction

The Arctic is warming about 4 times faster than the rest of the planet (Rantanen et al., 2022), a phenomenon called Arctic amplification (Serreze and Francis, 2006; Serreze and Barry, 2011), which has significant consequences both for the Arctic and across the globe (Serreze and Barry, 2011; Cohen et al., 2014; Coumou et al., 2018). The sea ice albedo feedback is a recognized and well-studied contributor to a disproportionately warming Arctic (Winton, 2006; Jenkins and Dai, 2021), leading directly to increased outgoing longwave radiation and turbulent heat fluxes from newly open ocean (Dai et al., 2019). However, processes in the lower atmosphere, which can indirectly contribute to Arctic warming and the way that warming is distributed, are poorly understood (Tjernström et al., 2012) and less frequently studied. This lack of understanding contributes to inaccuracies in the representation of present-day sea ice (Stroeve et al., 2012) and uncertainties in the state of the future Arctic climate in climate models (Hodson et al., 2012; Karlsson and Svensson, 2013; Cai et al., 2021). Determining the predominant thermodynamic structures and kinematic processes occurring in the Arctic lower atmosphere and how these relate to cloud characteristics and radiative transfer may help to constrain some of these uncertainties.

Insight into prevalent Arctic atmospheric processes can be gained by analysis of data collected during the MOSAiC (Multidisciplinary drifting Observatory for the Study of Arctic Climate) expedition (Shupe et al., 2020). MOSAiC was a year-long expedition that took place from October 2019 to September 2020 in which the research vessel *Polarstern* (Alfred-Wegener-Institut Helmholtz-Zentrum für Polar- und Meeresforschung, 2017) was frozen into the central Arctic Ocean sea ice pack and allowed to passively drift across the central Arctic for an entire year. During MOSAiC, a variety of instruments were deployed from the *Polarstern*, the section of sea ice approximately next to the *Polarstern* (hereafter called the MOSAiC floe), and at distances up to 40 km from the *Polarstern* (called the distributed network; Krumpen and Sokolov, 2020). A core goal of MOSAiC was to study key processes occurring in the atmosphere (Shupe et al., 2022), sea ice (Nicolaus et al., 2022), and ocean (Rabe et al., 2022) to understand Arctic climate change. Between October 2019 and mid-May 2020, the *Polarstern* drifted with the original MOSAiC ice floe. In mid-May, the *Polarstern* left the MOSAiC floe to conduct an exchange of people and equipment in Svalbard and then returned to the original MOSAiC floe in mid-June, where it remained until the end of July. At this point, the original MOSAiC floe disintegrated and so the *Polarstern* relocated to a newly identified ice floe near the North Pole, where it remained from late August through late September (Shupe et al., 2022).

The purpose of this paper is to summarize the methods used to develop a lower-atmospheric properties dataset (<https://doi.org/10.1594/PANGAEA.957760>, Jozef et al.,

2023) containing important information on several key atmospheric features, including the atmospheric boundary layer (ABL) height and stability, temperature inversion (TI) and low-level jet (LLJ) characteristics, near-surface meteorological state, cloud cover, and surface radiation budget over the span of an entire year in the Arctic. This lower-atmospheric properties dataset was developed by identifying features in all balloon-borne radiosondes, which were launched several times per day over the span of the MOSAiC year from the deck of the *Polarstern*, and supplemented by near-surface atmospheric data from a 10 m meteorological tower and surface radiation data from the radiation station located on the MOSAiC floe, as well as information on cloud cover from a ceilometer located on the deck of the *Polarstern*.

This paper does not delve into the physical significance of these observations. Rather, the goal is simply to explain the instrumentation (Sect. 2) and methods (Sect. 3) used to develop the accompanying lower-atmospheric properties dataset, with the expectation that the dataset will be useful to a wide variety of other projects.

2 Instrumentation

2.1 Radiosondes

The primary platform used to develop the lower-atmospheric properties dataset is the radiosonde. Throughout MOSAiC, radiosondes were launched from the stern deck of the *Polarstern* at least four times per day (every 6 h) for the entire year. These launches were typically conducted at 05:00, 11:00, 17:00, and 23:00 UTC (Maturilli et al., 2021). During events of particular interest, such as a warm-air intrusion event, or time spent sailing across the sea ice edge, radiosondes were launched up to eight times per day (every 3 h). Figure 1 shows the locations of each radiosonde launch throughout the expedition.

The balloon-borne Vaisala RS41 radiosondes used during MOSAiC measured temperature, pressure, relative humidity, and wind between the helicopter deck of the *Polarstern* (~12 m above the ice and depicted in Fig. 3 of Shupe et al., 2022) and about 30 km altitude (Maturilli et al., 2021). We use the level-2 radiosonde product (Maturilli et al., 2021) for the lower-atmospheric properties dataset as the level-2 radiosonde data are found to be more reliable in the lower troposphere than the level-3 radiosonde data (Maturilli et al., 2022). For the purpose of the lower-atmospheric properties dataset, we only use measurements up to 5 km as this is roughly the upper limit of the lower troposphere (Silva and Schlosser, 2021), and we are interested only in lower-atmospheric features. Radiosonde measurements were recorded with a frequency of 1 Hz, with a typical ascent rate of 5 m s^{-1} , resulting in measurements approximately every 5 m throughout the ascent. Information about instrumentation uncertainty can be found in Table 2. Radiosonde measurements were used to identify and characterize several key

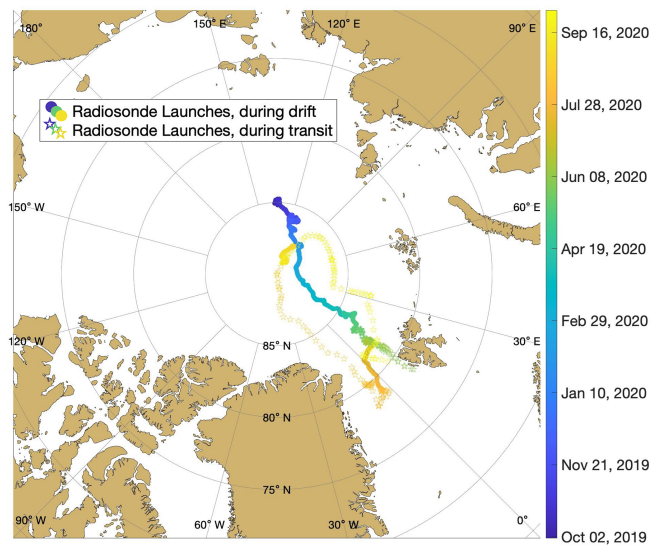


Figure 1. Map of the central Arctic showing the location of each radiosonde launch, color coded by date. Circular symbols indicate when the *Polarstern* was passively drifting, and star symbols indicate when the *Polarstern* was traveling under its own power.

features of the lower atmosphere, including ABL depth and stability and characteristics of TIs and LLJs. While the radiosonde profile is not an instantaneous snapshot of the atmosphere (it takes the radiosonde ~ 20 min to reach 5 km), the measurements can still provide a reasonable representation of the atmospheric state at the time of radiosonde launch, especially near the surface. Thus, all additional variables that were not derived directly from the radiosonde measurements are provided at the time of each radiosonde launch, presented as an average of values within approximately 5 min before and after launch (averaging interval is explained further throughout text).

Prior to processing the radiosonde data for integration into the lower-atmospheric properties dataset, radiosonde measurements were corrected to account for the local heat island resulting from the presence of the *Polarstern*. This local source of heat resulted in the frequent occurrence of elevated temperatures near the launch point, resulting in inconsistencies in the observed temperatures in the lowermost part of the atmosphere. This effect was found to frequently influence radiosonde measurements up to 23 m above sea level (11 m above the *Polarstern*'s helicopter deck), and in some cases, it was observed to extend even higher. This phenomenon can be recognized by a temperature structure indicative of a convective layer below 23 m. We know from previous literature that convective ABLs are rare in the central Arctic (Tjernström et al., 2004; Brooks et al., 2017); thus, it is unlikely that nearly all radiosondes would exhibit thermodynamic properties associated with convection near the surface. Therefore, this part of the profile is understood to be an artifact of the contamination and is thus considered to be unreliable. To mitigate

for this influence, all radiosonde measurements below 23 m were excluded. This helps in also removing faulty wind measurements that occur as a result of flow distortion around the ship (Achtert et al., 2015) and the radiosonde motion induced by the initial unraveling of the string that connects the radiosonde to the balloon.

If anomalously warm temperature measurements appeared to extend above 23 m (identified by continued presence of a convective atmosphere), then the lowest radiosonde measurements were visually compared to measurements from the 10 m meteorological tower to identify where temperature values were anomalously warm above 23 m. This was identifiable when the tower measurements interpolated upward, given their observed slope, did not match up with the radiosonde measurement at 23 m. The first credible value of the radiosonde measurements is found when the tower measurements interpolated upward line up with the observed radiosonde measurement or, in the case of a temperature offset between the tower and radiosonde, have the same slope. Data at the altitudes below this first credible value were removed.

An additional disruption of the radiosonde measurements sometimes occurred as a result of the passage of the balloon through the ship's exhaust plume. When it was unambiguous that the radiosonde passed through the ship's plume (made evident by a sharp increase and subsequent decrease in temperature, typically by ~ 0.5 – 1 °C over a vertical distance of ~ 10 – 30 m, identified visually), these values were replaced by values resulting from interpolation between the closest credible values above and below the anomalous measurements, which are identified as the last point just before the increase and the first point just after the decrease in temperature values, to acquire a continuous profile of reliable temperatures.

2.2 Meteorological tower

Near-surface data from the 10 m meteorological tower (hereafter called the met tower) are included to provide the near-surface context at the time when features identified in the radiosondes occurred since radiosonde measurements do not extend to the surface. The met tower was located on the sea ice at a site called Met City (Shupe et al., 2022), which was variable between 300 to 600 m from the *Polarstern* (Cox et al., 2023a, b) throughout the campaign. The met tower measurements included in the lower-atmospheric properties dataset were recorded at approximately 2 and 10 m above the surface of the sea ice (the true altitudes for each variable are shown in Table 1, where the given ranges account for varying snow depths). The values of variables from the met tower included in the lower-atmospheric properties dataset were determined using the 1 min met tower data (these data are reported as the average of the observations between the minute reported and the following minute – e.g., data at 12:30 UTC are an average of observations between 12:30 and 12:31 UTC), averaged between 5 min before and 5 min after

Table 1. True altitudes for met tower variables. Ranges in parentheses reflect the varying snow depth. n/a – not applicable.

Met tower variable	True 2 m height	True 10 m height
Temperature	1.75 m (1.1–2.2 m)	9.34 m (8.7–9.8 m)
Relative humidity	1.46 m (0.8–1.9 m)	9.14 m (8.5–9.6 m)
Pressure	1.65 m (1–2.1 m)	n/a
Wind	2.66 m (2–3.1 m)	10.54 m (9.9–11 m)

the time of launch, to avoid the potential for small fluctuations in the measurements at the time of radiosonde launch to misrepresent the true state of the atmosphere. This is carried out by determining the met tower time stamp closest in time to the radiosonde launch and averaging from 5 min before to 5 min after this time. For example, for a radiosonde launch time of 11:45:15 UTC, the corresponding met tower data are averaged between 11:40 and 11:50 UTC; as the data for 11:50 are the mean between 11:50 and 11:51 UTC, this results in data averaged over an 11 min period.

Temperature and relative humidity at the 10 m level were measured using a Vaisala HMT337, and at the 2 m level, they were measured using a Vaisala PTU307; atmospheric pressure was also observed at the 2 m sensor. Wind speed and direction were measured using a Metek uSonic-Cage MP sonic anemometer. Pressure at the 10 m level was approximated using the hypsometric equation (Stull, 1988). Information about instrumentation uncertainty can be found in Table 2.

In addition to providing metrics only recorded by the met tower, we also include some metrics calculated using data from both the met tower and radiosonde, specifically the bulk Richardson number and the change in virtual potential temperature calculated between 2 m from the met tower and the top of the ABL from the radiosondes (see Sect. 3.3). To improve the validity of such integrated quantities, work is in progress to interpolate between the tower and radiosonde measurements to create a continuous profile from the ground, which removes anomalous measurements in the radiosonde profiles resulting from the *Polarstern*'s heat island and exhaust plume effects.

While the radiosondes were launched at least four times per day throughout the entire MOSAiC year, met tower measurements were continuous when active; however, the met tower was not always active. This is because the met tower was located on the sea ice and needed constant power to run. Therefore, during transit periods or times when power to the met tower was cut, we do not have these near-surface measurements. The primary times in which we do not have met tower data are before 15 October 2019 (beginning of experiment), between 10 May and 7 June 2020 (*Polarstern* transit), between 29 July and 25 August 2020 (*Polarstern* transit), and after 18 September 2020 (end of experiment). Radiosonde and ceilometer measurements (Sect. 2.3) during these periods are relative to the position of the *Polarstern* and not to the position of the MOSAiC floe. Between the *Polarstern*

transit events, the met tower was installed in different locations (varying iterations of Met City) on the ice (three in total – the first two on the original ice floe and the third on the newly identified ice floe farther north), but each was always less than 600 m from the *Polarstern*.

2.3 Ceilometer

Information on cloud characteristics provided in the lower-atmospheric properties dataset comes from the Vaisala Ceilometer CL31 (ARM user facility, 2019) located on the P deck of the *Polarstern* (depicted in Fig. 3 of Shupe et al., 2022), deployed as part of the Department of Energy (DOE) Atmospheric Radiation Measurement (ARM) mobile facility suite (Shupe et al., 2021). The ceilometer measures atmospheric backscatter and cloud base height, which allows us to determine the altitude and presence of clouds during the time of radiosonde launch. The ceilometer measurements were recorded with a laser pulse rate of 10 kHz and averaged over 16 s. Information about instrumentation uncertainty can be found in Table 2. The utilized variables were determined using data averaged between approximately 5 min before and 5 min after the time of launch following the same time interval format as the met tower data. The averaging intervals vary due to the 16 s source data, but they are kept as small as possible while ensuring the aforementioned temporal spans. Intervals with less than 50 % data coverage are excluded from the follow-up calculations and marked as missing. Note that the altitude of the P deck was approximately 20 m above sea level, which could occasionally be above the presence of fog or blowing snow.

2.4 Radiation station

Information on surface radiation provided in the lower-atmospheric properties dataset comes from the DOE ARM radiation station located on the MOSAiC floe adjacent to the met tower at Met City (Shupe et al., 2022). This radiation station was outfitted with Eppley Precision Infrared Radiometers for measuring downwelling and upwelling broadband longwave radiation and Eppley Standard Precision Pyranometers for measuring downwelling and upwelling broadband shortwave radiation (Cox et al., 2023b). Information about instrumentation uncertainty can be found in Table 2. As with the met tower data, radiation station data were provided in 1 min intervals in Cox et al. (2023a) and were averaged in the same manner as the met tower and ceilometer data to report values at the time of the radiosonde launch in the current dataset. Prior to averaging, radiation measurements with values outside of a reasonable range (such as large values for shortwave radiation during polar night or negative values for any of the radiation components, explained further in Sect. 3.5) were excluded. During the times listed above in which the met tower was not taking measurements, we also do not have radiation station measurements.

Table 2. Variable uncertainty in the instrumentation used to derive the lower-atmospheric properties dataset.

Platform	Variable	Instrumentation	Uncertainty
Radiosonde	Pressure	Vaisala RS41-SGP	1.0 hPa (> 100 hPa), 0.6 hPa (< 100 hPa)
	Temperature		0.3 °C (< 16 km) 0.4 °C (> 16 km)
	Relative humidity		4 %
	Wind speed		0.15 m s ⁻¹
	Wind direction		2°
Met Tower	2 m temperature	Vaisala PTU307	0.3–0.4 °C
	2 m relative humidity		1.6 %–1.8 %
	2 m pressure		0.15 hPa
	10 m temperature	Vaisala HMT337	0.3–0.4 °C
	10 m relative humidity		1.6 %–1.8 %
	2 and 10 m wind speed	Metek uSonic-Cage MP sonic anemometer	0.3 m s ⁻¹
	2 and 10 m wind direction		2°
Ceilometer	Cloud base height	Vaisala CL31	5 m
Radiation station	Longwave radiation	Eppley Precision Infrared Radiometer	2.6 W m ⁻² (downwelling) 1 W m ⁻² (upwelling)
	Shortwave radiation	Eppley Standard Precision Pyranometer	4.5 W m ⁻²

3 Variables included in the lower-atmospheric properties dataset

3.1 Temperature

The temperature-related variables provided in the lower-atmospheric properties dataset include temperature inversion characteristics, as well as temperature (and pressure) from the met tower and at the ABL top (derivation of ABL height is discussed in Sect. 3.3).

To identify a TI layer, we refer to a profile of the temperature gradient (dT/dz) for each case. dT/dz is calculated across 30 m intervals in steps of 5 m and attributed to the center altitude of Δz (i.e., 23–53, 28–58, 33–63 m, and so on, resulting in a dT/dz profile with values at 38, 43, 48 m a.g.l. and so on) between the bottom of the radiosonde profile and 5 km. We then determine the presence of a TI layer by identifying where dT/dz exceeds a threshold of $0.65\text{ °C}(100\text{ m})^{-1}$. Previous work by Kahl (1990) and Gilson et al. (2018) used a threshold of $0\text{ °C}(100\text{ m})^{-1}$; however, we find that a threshold of $0.65\text{ °C}(100\text{ m})^{-1}$ is better suited for the fine-scale vertical resolution of the radiosonde data. In 28 % of cases, using a threshold of 0.65 instead of $0\text{ °C}(100\text{ m})^{-1}$ does not make a difference in terms of what is identified as a TI layer. However, in most instances, using the higher threshold is critical. If we use a threshold of 0 °C

$(100\text{ m})^{-1}$ and identify anywhere where dT/dz exceeds this threshold as a TI (Kahl, 1990), then we can incorrectly identify a nearly isothermal layer as a TI. Using a threshold of $0.65\text{ °C}(100\text{ m})^{-1}$, which has been tested amongst other options and deemed to identify TIs most accurately, prevents this.

We include two additional criteria when identifying TI layers. First, we only identify sections of the profile in which dT/dz stays above the threshold of $0.65\text{ °C}(100\text{ m})^{-1}$ for at least 25 m as TIs to avoid including measurement artifacts or highly localized temperature variability. Second, if dT/dz goes below the threshold for less than 100 m between two TI layers, then these layers are combined into a single TI layer for the current dataset (Kahl, 1990; Tjernström and Graversen, 2009; Gilson et al., 2018).

Once we have identified all TIs within a profile, we determine the depth of each TI as the vertical distance between the TI bottom and top and the intensity of the TI as the difference between the temperatures at the TI bottom and top (Gilson et al., 2018). Figure 2 shows an example of our TI identification method, as well as the depth and intensity of the TIs identified.

In the lower-atmospheric properties dataset accompanying this paper, the metrics for all TIs found in each radiosonde profile are included in the variables called `inv_alt` (altitude

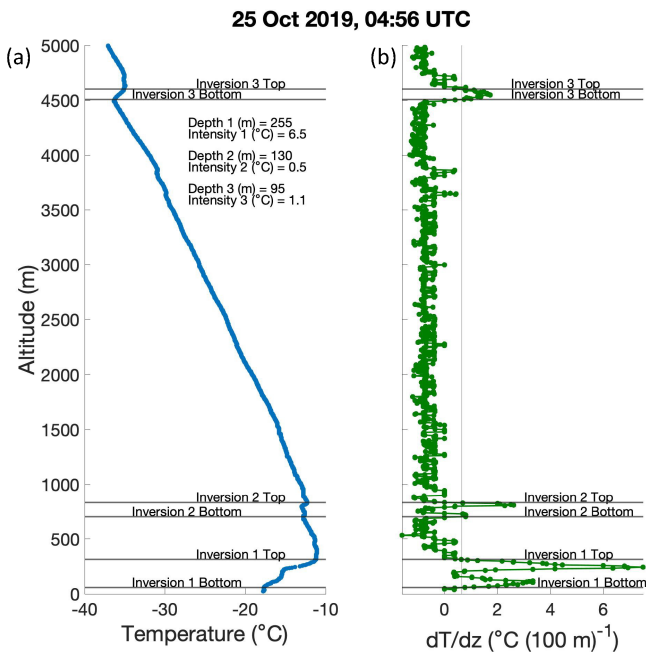


Figure 2. Example of temperature inversion identification using radiosonde profile at 04:56 UTC on 25 October 2019. Horizontal black lines on the (a) temperature profile and (b) dT/dz profile indicate the bottom and top of each TI. Vertical black line on the dT/dz profile indicates the threshold of $0.65\text{ °C (100 m)}^{-1}$. The depth and intensity of each inversion are written on the temperature profile plot.

of the bottom of the TI), inv_t (temperature at the bottom of the TI), inv_dt (TI intensity), and inv_dz (TI depth). These variables are provided as multidimensional matrices so that information about all inversions in a given profile, for all profiles, is provided in one variable, with the maximum number of TIs in any one profile being nine. Note that, while the presence and strength of temperature inversions may be relevant for some applications related to static stability, a user is encouraged to utilize metrics provided in Sect. 3.3 or to calculate the potential temperature gradient for a case of interest for a better description of stability.

Additional temperature variables included in the lower-atmospheric properties dataset described by this paper are the temperature at 2 and 10 m from the met tower (t_2m and t_10m , respectively), as well as temperature at the top of the ABL from the radiosonde profiles (t_h). In addition, pressure at 2 m, 10 m, and the ABL top are provided so that a user can calculate potential temperature at these altitudes (p_2m , p_10m , and p_h , respectively).

3.2 Wind

The wind-related variables provided in the lower-atmospheric properties dataset include low-level jet characteristics, as well as zonal and meridional wind speeds from the met tower and at the ABL top.

Using the wind speed profile, we identify an LLJ as a maximum in the wind speed that is at least 2 m s^{-1} greater than the wind speed minima above and below (Stull, 1988). As described in Tuononen et al. (2015), only situations in which both the wind speed maximum (the LLJ core) and the minimum above the core are both below 1500 m are identified as LLJs. Above this altitude, a wind speed maximum is unlikely to be related to surface processes and is more likely to be synoptic in nature. If an LLJ is found, we identify the LLJ core altitude as the altitude of the maximum in the wind speed (llj_alt), the LLJ speed as the wind speed at that altitude (llj_spd) (Jakobson et al., 2013), and the LLJ direction as the wind direction at that altitude (llj_dir). Additionally, we identify the LLJ top as the altitude of the minimum in the wind speed profile above the LLJ. The altitude difference between the LLJ core and top is then the LLJ depth (llj_dz), and the difference between the wind speed at the LLJ core and top is then the LLJ strength (llj_dv) (Jakobson et al., 2013).

In Tuononen et al. (2015) an additional criterion is applied to LLJ identification, in which only a wind speed maximum that is at least 25 % faster than the wind speed at the minimum above is identified as an LLJ. In the lower-atmospheric properties dataset, we include an LLJ flag (llj_flag), which indicates whether the 25 % criterion is met ($llj_flag = 1$) or not ($llj_flag = 0$). Most instances in which the 25 % criterion is not fulfilled are examples in which the wind speed throughout the entire profile is very fast so the wind speed above the LLJ core decreases by 2 m s^{-1} but not by 25 %. We include all LLJs, as well as indicate which ones meet this 25 % criterion, to allow the user to choose which identification method is relevant to their application of the lower-atmospheric properties dataset. Figure 3 shows two examples of our LLJ identification method, one in which $llj_flag = 1$ and one in which $llj_flag = 0$, as well as how the depth and strength of the LLJ are calculated. Lopez-Garcia et al. (2022) presents an analysis of MOSAiC LLJ frequency and forcing mechanisms using only LLJs in which the 25 % criterion is met; thus, their analysis is consistent with the LLJ characteristics presented in the lower-atmospheric properties dataset when $llj_flag = 1$.

Additional wind variables included in the lower-atmospheric properties dataset accompanying this paper are zonal and meridional wind speed at 2 and 10 m from the met tower. Zonal wind speed variables are called u_2m and u_10m , respectively, and meridional wind speed variables are called v_2m and v_10m , respectively. Wind speed components at the ABL top measured by the radiosonde are also included (u_h and v_h). Wind is provided in components for ease of calculating a gradient or a temporal or spatial average

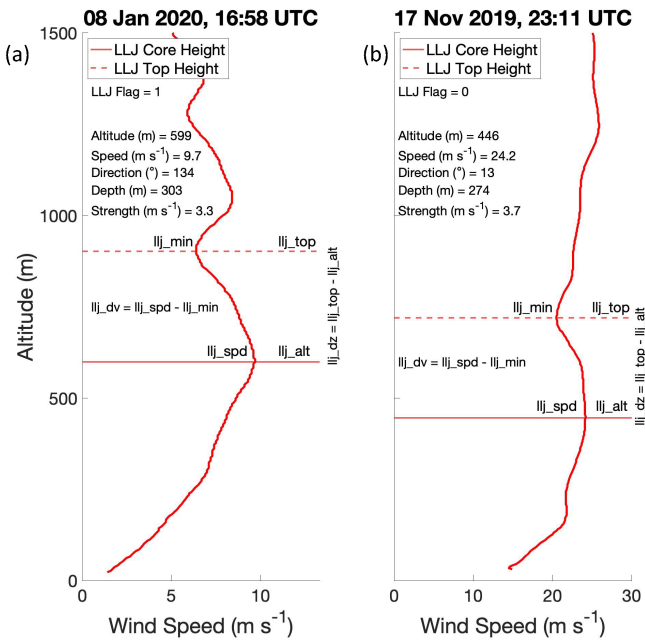


Figure 3. Example of low-level jet identification using radiosonde profiles at (a) 16:58 UTC on 8 January 2020, where $llj_flag = 1$, and (b) 23:11 UTC on 17 November 2019, where $llj_flag = 0$. The horizontal solid red line indicates the altitude of the LLJ core (llj_alt), and the horizontal dashed red line indicates the altitude of the top of the LLJ (llj_top). The speed of the LLJ is indicated by llj_spd , and the speed at the top of the LLJ is indicated by llj_min . The processes of calculating LLJ depth (llj_dz) and strength (llj_dv) are shown, and all relevant LLJ characteristics are written on both plots.

of wind direction. Total wind speed and wind direction can be calculated from the components if this is of interest.

3.3 Stability

The stability-related variables provided in the lower-atmospheric properties dataset include ABL height, the stability regime from both the met tower and the lowest portion of the radiosonde measurements, and the bulk Richardson number (Ri_b) and change in virtual potential temperature ($d\theta_v$) calculated over three depths: between 2 and 10 m, between the lowest radiosonde measurement and the ABL top, and between 2 m and the ABL top.

The ABL is the turbulent lowest part of the atmosphere that is directly influenced by the Earth’s surface (Stull, 1988; Marsik et al., 1995). Ri_b is the ratio between buoyant and mechanical turbulent forcings (Sivaraman et al., 2013) and can help to identify the top of the ABL under the assumption that turbulence ceases above the ABL (Stull, 1988); thus, Ri_b will exceed a critical value at the top of the ABL (Seibert et al., 2000). To identify ABL height (h), we apply a Ri_b -based approach in which the top of the ABL is identified as the first altitude at which Ri_b exceeds a critical value of 0.5 and

remains above the critical value for at least 20 consecutive meters (Jozef et al., 2022).

Ri_b is calculated using the following equation from Stull (1988):

$$Ri_b(z) = \frac{\left(\frac{g}{\bar{\theta}_v}\right) \Delta\theta_v \Delta z}{\Delta u^2 + \Delta v^2}, \quad (1)$$

where g is acceleration due to gravity, $\bar{\theta}_v$ is the mean virtual potential temperature over the altitude range being considered, z is altitude, u is zonal wind speed, v is meridional wind speed, and Δ represents the difference over the altitude range used to calculate Ri_b throughout the profile. Ri_b profiles are created by calculating Ri_b across 30 m intervals in steps of 5 m and attributing the resulting Ri_b value to the center altitude of Δz (i.e., 23–53, 28–58, 33–63 m, and so on, resulting in a Ri_b profile with values at 38, 43, 48 m a.g.l., and so on) rather than using the ground as the reference level in order to isolate the local likelihood of turbulence rather than that over the full depth from the surface (Stull, 1988; Georgoulas et al., 2009; Dai et al., 2014). Figure 4 demonstrates an example of how ABL height is found using this Ri_b -based approach. Due to these methods, we cannot identify an ABL height below a minimum of 38 m (this value may be higher if the bottom altitude of the radiosonde profile is above 23 m). However, in the case there is a very shallow ABL due to a surface-based or low-level inversion, this is detected in the first layer of Ri_b , and thus, the ABL height is still determined to be shallow.

In addition to the ABL height, we also provide the stability regime (1 is the stable boundary layer (SBL), 2 is the neutral boundary layer (NBL), and 3 is the convective boundary layer (CBL)) captured by the radiosonde, as well as by the met tower. We provide both as 45 % of the time the stability of the surface layer, recorded by the met tower, was different than that of the remaining ABL, recorded by the radiosonde. The stability regimes from the radiosondes ($s_radiosonde$) and tower (s_tower) are determined by the following equations (adapted from Liu and Liang, 2010, and Jozef et al., 2022), which compare θ_v between the upper and lower bounds of an altitude range spanning the lower atmosphere.

$$\theta_{v_upper} - \theta_{v_lower} < -\delta_s = \text{CBL} \quad (2)$$

$$\theta_{v_upper} - \theta_{v_lower} > +\delta_s = \text{SBL} \quad (3)$$

$$-\delta_s \leq \theta_{v_upper} - \theta_{v_lower} \leq +\delta_s = \text{NBL} \quad (4)$$

$$\delta_s = \frac{0.2 \text{ K}}{40 \text{ m}} \Delta z \quad (5)$$

$$\Delta z \approx 30 \text{ m (for } s_radiosonde)$$

$$\Delta z = 7.59 \text{ m (for } s_tower)$$

Here, δ_s is a stability threshold that represents the minimum θ_v increase (decrease) with altitude near the surface neces-

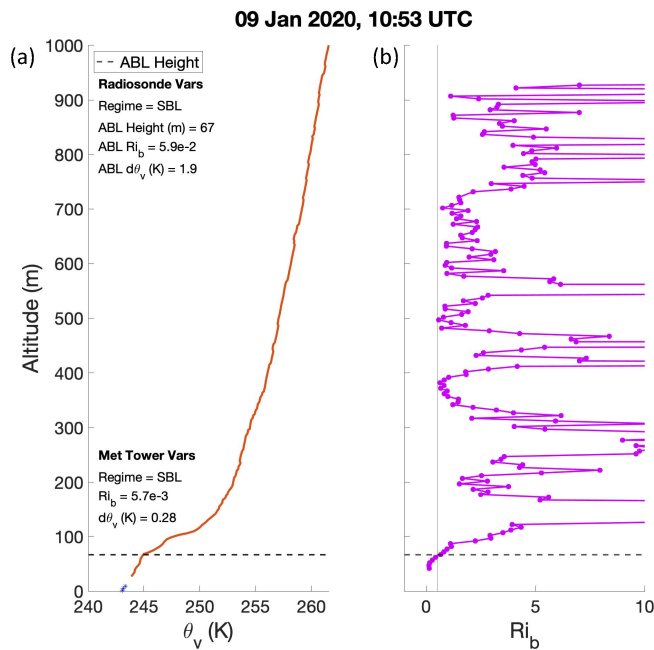


Figure 4. Example of atmospheric boundary layer height identification using radiosonde profiles at 10:53 UTC on 9 January 2020, where the orange line is radiosonde data, and the near-surface blue asterisks are met tower data in (a). Horizontal dashed black lines on the (a) virtual potential temperature profile and (b) Ri_b profile indicate the ABL height, which is also written on the left panel. The stability regime, Ri_b , and $d\theta_v$ calculated using both the radiosonde and met tower data are written on the left panel.

sary for the ABL to qualify as an SBL (CBL). If this minimum is not reached in either direction, the ABL is identified as an NBL (Liu and Liang, 2010). For profiles over the ocean and/or ice, Liu and Liang (2010) define δ_s to be 0.2 K. Jozef et al. (2022) found that, for shallow Arctic ABLs, comparing the θ_v change over the lowest 40 m of the profile ($\theta_{v_{\text{lower}}} = \theta_{v_{5\text{m}}}$ and $\theta_{v_{\text{upper}}} = \theta_{v_{45\text{m}}}$) to this stability threshold gives the best estimate of stability regime. Since there are no valid radiosonde observations in any given profile as low as 5 m, and many radiosondes record their lowest good value around 25 m, we adapt the methods presented in Jozef et al. (2022) discussed above to instead compare θ_v change over the lowest 30 m ($\theta_{v_{\text{lower}}} = \theta_{v_i}$ to $\theta_{v_{\text{upper}}} = \theta_{v_{i+30\text{m}}}$) recorded by the radiosonde for determination of radiosonde stability regime. However, since radiosonde measurements are not taken at the same altitudes in every profile, we use the altitude range closest to 30 m as possible, but this may vary slightly from profile to profile. Therefore, we use the true Δz to calculate a unique δ_s for each profile, given Eq. (5). When the top of the ABL is less than 30 m above the lowest radiosonde measurement, we determine the stability regime using Δz as the distance in meters between the lowest radiosonde measurement and the top of the ABL.

The stability regime from the met tower is found using the altitude range of $\theta_{v_{\text{lower}}} = \theta_{v_{2\text{m}}}$ to $\theta_{v_{\text{upper}}} = \theta_{v_{10\text{m}}}$, which calculates δ_s using $\Delta z = 7.59$ m as this is the true distance between met tower measurements at 2 and 10 m, indicated by Table 1.

Additional metrics provided for stability in the lower-atmospheric properties dataset are Ri_b and $d\theta_v$ calculated over different distances in the near-surface layer of the atmosphere. First, Ri_b and $d\theta_v$ between 2 and 10 m are provided in variables called `rib_tower` and `dptv_tower`, respectively, calculated using data from the met tower where a positive value for $d\theta_v$ indicates that virtual potential temperature at 10 m is greater than that at 2 m. Next, Ri_b and $d\theta_v$ between the bottom of the radiosonde profile and the top of the ABL are provided in variables called `rib_radiosonde` and `dptv_radiosonde`, respectively. Finally, Ri_b and $d\theta_v$ between 2 m from the met tower and the top of the ABL from the radiosonde are provided in variables called `rib_2m_h` and `dptv_2m_h`, respectively.

3.4 Moisture

The moisture-related variables provided in the lower-atmospheric properties dataset include the altitude of the lowest cloud base, the percentage of time in the 5 min before and after the radiosonde launch in which there are clouds (general cloud cover), the percentage of the time in the 5 min before and after the radiosonde launch in which there are clouds at or below the ABL height (ABL cloud cover), and the mixing ratio measured at the met tower and at the ABL top.

Cloud variables are determined using ceilometer data. First, the altitude of the lowest cloud base (`cbh`) is determined by calculating the average of all the valid observed lowest cloud base heights in the observation interval (approximately 5 min before to 5 min after radiosonde launch). If there is any period of clear sky during this interval, the clear-sky period is excluded from the calculation of the mean.

Next, general cloud cover (`cc`) is calculated first by determining if there is any cloud base height detected in the observational interval. Then, we count the number of observations within the observational interval in which there are clouds detected and divide this by the total number of observations in the interval. Lastly, ABL cloud cover (`cc_h`) is estimated by counting the number of observations in the interval in which cloud cover is detected at or below the ABL top and dividing this by the total number of observations in the interval. Since the ceilometer is located on the deck of the *Polarstern*, this method likely misses fog events. For the presence of fog, the “present weather” variable in Schmithüsen and Raeke (2021a, b, c) can be used, although this information on fog is not included in the lower-atmospheric properties dataset.

Finally, we provide the mixing ratio at 2 and 10 m measured by the met tower (r_{2m} and r_{10m} , respectively) and at the top of the ABL measured by the radiosonde (r_h).

3.5 Radiation

The radiation-related variables provided in the lower-atmospheric properties dataset include surface upwelling and downwelling broadband longwave and broadband shortwave irradiance, measured by the radiation station located on the MOSAiC floe. For cases in which the sun was below the horizon, the shortwave irradiance recorded may have been a small positive or negative number due to instrument uncertainty when the true irradiance is zero. To mitigate this, we set the average shortwave irradiance over the observational interval to zero if the average solar zenith angle $> 93^\circ$ (the sun is below the horizon, and diffuse radiation is negligible) or if the average shortwave irradiance is negative.

The upwelling and downwelling broadband longwave irradiance variables are called $lwup$ and $lwdn$, respectively, and the upwelling and downwelling broadband shortwave irradiance variables are called $swup$ and $swdn$, respectively. A user may refer to these values to help calculate total upwelling and downwelling radiation, as well as the surface net radiation.

4 Summary of the lower-atmospheric properties dataset

Table 3 below summarizes the name of each variable included in the lower-atmospheric properties dataset, the quantity it measures (including units), and the platform from which the data came. In addition to the atmospheric properties included in the table, the lower-atmospheric properties dataset also includes the latitude (lat), longitude (lon), and time ($time$) of each radiosonde launch in seconds since Epoch.

For all variables in the lower-atmospheric properties dataset, missing values are given the `_FillValue` and `missing_value` attributes of `-9999`. When the platform listed in Table 3 is tower or radstat, a missing value means that the tower or radiation measurement was not taken, respectively. When the platform listed in Table 3 is the combined sonde-tower, a missing value means that the tower measurement needed to determine the quantity was not taken. When the platform listed in Table 3 is sonde, a missing value indicates that the feature was not present, though the measurement was still taken (e.g., a missing value for `llj_alt` or `inv_alt` indicates there was no LLJ or TI present in the observation, respectively). For the ceil observations, times when cloud measurements were taken but clouds were not present can be identifiable when there is a missing value for `cbh` and when `cc = 0`. When there is a missing value for both `cbh` and `cc`, then no cloud measurement was taken.

5 Data availability

The lower-atmospheric properties dataset described in this paper is available at the PANGAEA Data Publisher at <https://doi.org/10.1594/PANGAEA.957760> (Jozef et al., 2023). Level-2 radiosonde data used to develop the lower-atmospheric properties dataset are available at the PANGAEA Data Publisher at <https://doi.org/10.1594/PANGAEA.928656> (Maturilli et al., 2021). Near-surface atmospheric data from the meteorological tower and data from the radiation station are available at the National Science Foundation Arctic Data Center at <https://doi.org/10.18739/A2PV6B83F> (Cox et al., 2023a) as described in Cox et al. (2023b). Ceilometer data are available at the Department of Energy Atmospheric Radiation Measurement Data Center at <https://doi.org/10.5439/1181954> (ARM user facility, 2019).

6 Conclusions

The quantities in the lower-atmospheric properties dataset are based on data from 1509 radiosonde profiles, launched between 1 October 2019 and 1 October 2020 at latitudes between 78.36 and 90° N. A wide variety of atmospheric conditions were sampled throughout the MOSAiC year, which will aid interested researchers in understanding the complex interactions between lower-atmospheric processes in the central Arctic and their impact on future climate change.

Atmospheric observations from the MOSAiC expedition provide novel insights into the thermodynamic and kinematic processes prevalent in the lower Arctic atmosphere through the merging of disparate yet complementary in situ observations. This paper summarizes a dataset that includes information about key atmospheric features observed over the span of an entire year in the central Arctic: the atmospheric boundary layer, temperature inversions, and low-level jets. The lower-atmospheric properties dataset also includes information about the state of the near-surface atmosphere, cloud cover, and surface radiation budget. While this paper does not delve into the physical significance of the variables included in the lower-atmospheric properties dataset, the authors intend for this dataset to be used for a wide variety of applications, including identifying certain times in which features of interest occurred, putting other data into perspective with an understanding of the atmospheric state throughout the year or comparing the characteristics of different features to each other, with the overall goal of gaining a greater understanding of the atmospheric processes governing the central Arctic and how they may contribute to future climate change.

Author contributions. GCJ, RR, JJC, GdB, and BM conceptualized the analysis presented in this paper; SD provided the radiosonde data; CJC provided the meteorological tower and radiation data; GCJ analyzed the radiosonde, met tower, and radiation

Table 3. List of variable descriptions, names, and units and the platform from which they were derived as included in the lower-atmospheric properties dataset summarized in this paper. Platform name sonde refers to the radiosondes, tower refers to the 10 m meteorological tower, ceil refers to the ceilometer, and radstat refers to the radiation station.

	Atmospheric property	Variable	Units	Platform	
Temperature	Temperature at 2 m altitude	t_2m	°C	tower	
	Temperature at 10 m altitude	t_10m	°C	tower	
	Temperature at ABL top	t_h	°C	sonde	
	Pressure at 2 m altitude	p_2m	hPa	tower	
	Pressure at 10 m altitude	p_10m	hPa	tower	
	Pressure at ABL top	p_h	hPa	sonde	
	Lower boundary of each temperature inversion	inv_alt	m	sonde	
	Lower-boundary temperature of each temperature inversion	inv_t	°C	sonde	
	Intensity of each temperature inversion	inv_dt	°C	sonde	
	Depth of each temperature inversion	inv_dz	m	sonde	
Wind	Zonal wind at 2 m altitude	u_2m	m s ⁻¹	tower	
	Zonal wind at 10 m altitude	u_10m	m s ⁻¹	tower	
	Zonal wind at ABL top	u_h	m s ⁻¹	sonde	
	Meridional wind at 2 m altitude	v_2m	m s ⁻¹	tower	
	Meridional wind at 10 m altitude	v_10m	m s ⁻¹	tower	
	Meridional wind at ABL top	v_h	m s ⁻¹	sonde	
	Low-level jet core altitude	llj_alt	m	sonde	
	Low-level jet core speed	llj_spd	m s ⁻¹	sonde	
	Low-level jet core direction	llj_dir	°	sonde	
	Low-level jet depth	llj_dz	m	sonde	
	Low-level jet strength	llj_dv	m s ⁻¹	sonde	
		Low-level jet flag	llj_flag	unitless	sonde
	Stability	$\Delta\theta_v$ between 2 m altitude and 10 m altitude	dptv_tower	K	tower
$\Delta\theta_v$ over the radiosonde data up to ABL top		dptv_sonde	K	sonde	
$\Delta\theta_v$ between 2 m altitude and ABL top		dptv_2m_h	K	sonde–tower	
ABL top		h	m	sonde	
Ri_b between 2 m altitude and 10 m altitude		rib_tower	unitless	tower	
Ri_b over the radiosonde data up to ABL top		rib_sonde	unitless	sonde	
Ri_b between 2 m altitude and 10 m altitude		rib_2m_h	unitless	sonde–tower	
Stability regime based on tower data		s_tower	unitless	tower	
	Stability regime based on radiosonde data	s_sonde	unitless	sonde	
Moisture	Lowest cloud base altitude	cbh	m	ceil	
	Cloud cover	cc	# out of 1	ceil	
	ABL cloud cover	cc_h	# out of 1	ceil	
	Mixing ratio at 2 m altitude	r_2m	g kg ⁻¹	tower	
	Mixing ratio at 10 m altitude	r_10m	g kg ⁻¹	tower	
	Mixing ratio at ABL top	r_h	g kg ⁻¹	sonde	
Radiation	Longwave downwelling radiative flux	lwdn	W m ⁻²	radstat	
	Longwave upwelling radiative flux	lwup	W m ⁻²	radstat	
	Shortwave downwelling radiative flux	swdn	W m ⁻²	radstat	
	Shortwave upwelling radiative flux	swup	W m ⁻²	radstat	

data; RR analyzed the ceilometer data; GdB, JJC, RR, SD, and CJC provided feedback on the analysis techniques; GJ wrote the paper; RR, GdB, JJC, BM, SD, and CJC reviewed and edited the paper.

Competing interests. The contact author has declared that none of the authors has any competing interests.

Disclaimer. Publisher's note: Copernicus Publications remains neutral with regard to jurisdictional claims made in the text, published maps, institutional affiliations, or any other geographical representation in this paper. While Copernicus Publications makes every effort to include appropriate place names, the final responsibility lies with the authors.

Acknowledgements. Data used in this paper were produced as part of the RV *Polarstern* cruise AWI_PS122_00 and as part of the international Multidisciplinary drifting Observatory for the Study of the Arctic Climate (MOSAiC) with the tag MOSAiC20192020. We thank all those who contributed to MOSAiC and made this endeavor possible (Nixdorf et al., 2021). Radiosonde data were obtained through a partnership between the leading Alfred Wegener Institute (AWI), the Atmospheric Radiation Measurement (ARM) User Facility, a US Department of Energy (DOE) facility managed by the Biological and Environmental Research Program, and the German Weather Service (DWD). Meteorological tower data were obtained by the National Oceanic and Atmospheric Administration (NOAA). Ceilometer data were obtained by the AWI and DOE-ARM User Facility. Radiation data were obtained by the DOE-ARM User Facility. We appreciate the comments provided by an anonymous internal reviewer at NOAA.

Financial support. Funding support for this analysis was provided by the National Science Foundation (award no. OPP-1805569, de Boer, PI), the National Aeronautics and Space Administration (award no. 80NSSC19M0194), and the German Federal Ministry of Education and Research (award no. 03F0871A). The meteorological tower and radiation station observations were supported by the National Science Foundation (no. OPP-1724551), by NOAA's Physical Sciences Laboratory (PSL) (NOAA Cooperative Agreement no. NA22OAR4320151) and by NOAA's Global Ocean Monitoring and Observing Program (GOMO)/Arctic Research Program (ARP) (FundRef <https://doi.org/10.13039/100018302>, NOAA's Global Ocean Monitoring and Observing Program, 2021). Additional funding and support were provided by the Department of Atmospheric and Oceanic Sciences at the University of Colorado Boulder, the Cooperative Institute for Research in Environmental Sciences, the National Oceanic and Atmospheric Administration Physical Sciences Laboratory, and the Alfred Wegener Institute.

Review statement. This paper was edited by Guanyu Huang and reviewed by Ian Brooks and one anonymous referee.

References

- Achtert, P., Brooks, I. M., Brooks, B. J., Moat, B. I., Prytherch, J., Persson, P. O. G., and Tjernström, M.: Measurement of wind profiles by motion-stabilised ship-borne Doppler lidar, *Atmos. Meas. Tech.*, 8, 4993–5007, <https://doi.org/10.5194/amt-8-4993-2015>, 2015.
- Alfred-Wegener-Institut Helmholtz-Zentrum für Polar- und Meeresforschung: Polar Research and Supply Vessel POLARSTERN operated by the Alfred-Wegener-Institute, *J. Large-Scale Res. Facil.*, 3, 1–8, <https://doi.org/10.17815/jlsrf-3-163>, 2017.
- Atmospheric Radiation Measurement (ARM) user facility: Ceilometer (CEIL), 2019-10-11 to 2020-10-01, ARM Mobile Facility (MOS) MOSAIC (Drifting Obs – Study of Arctic Climate), AMF2 (M1), compiled by: Morris, V., Zhang, D., and Ermold, B., ARM Data Center [data set], <https://doi.org/10.5439/1181954>, 2019.
- Brooks, I. M., Tjernström, M., Persson, P. O. G., Shupe, M. D., Atkinson, R. A., Canut, G., Birch, C. E., Mauritsen T., Sedlar, J., and Brooks, B. J.: The Turbulent Structure of the Arctic Summer Boundary Layer During The Arctic Summer Cloud-Ocean Study, *J. Geophys. Res.-Atmos.*, 122, 9685–9704, <https://doi.org/10.1002/2017JD027234>, 2017.
- Cai, Z., You, Q., Wu, F., Chen, H. W., Chen, D., and Cohen, J.: Arctic Warming Revealed by Multiple CMIP6 Models: Evaluation of Historical Simulations and Quantification of Future Projection Uncertainties, *J. Climate*, 34, 4871–4892, <https://doi.org/10.1175/JCLI-D-20-0791.1>, 2021.
- Cohen, J., Screen, J., Furtado, J., Barlow, M., Whittleston, D., Coumou, D., Francis, J., Dethloff, K., Entekhabi, D., Overland, J., and Jones, J.: Recent Arctic amplification and extreme mid-latitude weather, *Nat. Geosci.*, 7, 627–637, <https://doi.org/10.1038/NGEO2234>, 2014.
- Coumou, D., Di Capua, G., Vavrus, S., Wang, L., Wang, S.: The influence of Arctic amplification on mid-latitude summer circulation, *Nat. Commun.*, 9, 2959, <https://doi.org/10.1038/s41467-018-05256-8>, 2018.
- Cox, C. J., Gallagher, M., Shupe, M., Persson, O., Blomquist, B., Grachev, A., Riihimaki, L., Kutchenreiter, M., Morris, V., Solomon, A., Brooks, I., Costa, D., Gattas, D., Hutchings, J., Osborn, J., Morris, S., Preusser, A., and Uttal, T.: Met City meteorological and surface flux measurements (Level 3 Final), Multidisciplinary Drifting Observatory for the Study of Arctic Climate (MOSAiC), central Arctic, October 2019–September 2020, Arctic Data Center [data set], <https://doi.org/10.18739/A2PV6B83F>, 2023a.
- Cox, C. J., Gallagher, M., Shupe, M. D., Persson, P. O. G., Solomon, A., Fairall, C. W., Ayers, T., Blomquist, B., Brooks, I. M., Costa, D., Grachev, A., Gattas, D., Hutchings, J. K., Kutchenreiter, M., Leach, J., Morris, S. M., Morris, V., Osborn, J., Pezoa, S., Preusser, A., Riihimaki, L., and Uttal, T.: Continuous observations of the surface energy budget and meteorology over the Arctic sea ice during MOSAiC, *Sci. Data*, 10, 519, <https://doi.org/10.1038/s41597-023-02415-5>, 2023b.
- Dai, C., Wang, Q., Kalogiros, J. A., Lenschow, D. H., Gao, Z., and Zhou, M.: Determining Boundary-Layer Height from Aircraft Measurements, *Bound.-Lay. Meteorol.*, 152, 277–302, <https://doi.org/10.1007/s10546-014-9929-z>, 2014.

- Dai, A., Luo, D., Song, M., and Liu, J.: Arctic amplification is caused by sea-ice loss under increasing CO₂, *Nat. Commun.*, 10, 121, <https://doi.org/10.1038/s41467-018-07954-9>, 2019.
- Georgoulas A. K., Papanastasiou, D. K., Melas, D., Amiridis, V., and Alexandri, G.: Statistical analysis of boundary layer heights in a suburban environment, *Meteorol. Atmos. Phys.*, 104, 103–111, <https://doi.org/10.1007/s00703-009-0021-z>, 2009.
- Gilson, G. F., Jiskoot, H., Cassano, J. J., and Nielson, T. R.: Radiosonde-Derived Temperature Inversions and their Association with Fog over 37 Melt Seasons in East Greenland, *J. Geophys. Res.-Atmos.*, 123, 9571–9588, <https://doi.org/10.1029/2018JD028886>, 2018.
- Hodson, D. L. R., Keeley, S. P. E., West, A., Ridley, J., Hawkins, E., and Hewitt, H. T.: Identifying uncertainties in Arctic climate change projections, *Clim. Dynam.*, 40, 2849–2865, <https://doi.org/10.1007/s00382-012-1512-z>, 2012.
- Jakobson, L., Vihma, T., Jakobson, E., Palo, T., Männik, A., and Jaagus, J.: Low-level jet characteristics over the Arctic Ocean in spring and summer, *Atmos. Chem. Phys.*, 13, 11089–11099, <https://doi.org/10.5194/acp-13-11089-2013>, 2013.
- Jenkins, M. and Dai, A.: The impact of sea-ice loss on Arctic climate feedbacks and their role for Arctic amplification, *Geophys. Res. Lett.*, 48, e2021GL094599, <https://doi.org/10.1029/2021GL094599>, 2021.
- Jozef, G., Cassano, J., Dahlke, S., and de Boer, G.: Testing the efficacy of atmospheric boundary layer height detection algorithms using uncrewed aircraft system data from MOSAiC, *Atmos. Meas. Tech.*, 15, 4001–4022, <https://doi.org/10.5194/amt-15-4001-2022>, 2022.
- Jozef, G., Klingel, R., Cassano, J., Maronga, B., de Boer, G., Dahlke, S., and Cox, C.: Lower atmospheric properties relating to temperature, wind, stability, moisture, and surface radiation budget over the central Arctic sea ice during MOSAiC, PANGAEA [data set], <https://doi.org/10.1594/PANGAEA.957760>, 2023.
- Kahl, J.: Characteristics of the Low-level Temperature Inversion along the Alaskan Arctic Coast, *Int. J. Climatol.*, 10, 537–548, 1990.
- Karlsson, J. and Svensson, G.: Consequences of Poor Representation of Arctic Sea-ice Albedo and Cloud-radiation Interactions in the CMP5 Model Ensemble, *Geophys. Res. Lett.*, 40, 4374–4379, <https://doi.org/10.1002/grl.50768>, 2013.
- Kruppen, T. and Sokolov, V.: The Expedition AF122/1: Setting up the MOSAiC Distributed Network in October 2019 with Research Vessel AKADEMIK FEDOROV, *Berichte zur Polar- und Meeresforschung = Reports on polar and marine research*, Bremerhaven, Alfred Wegener Institute for Polar and Marine Research, 744, 119 pp., https://doi.org/10.2312/BzPM_0744_2020, 2020.
- Liu, S. and Liang, X. Z.: Observed Diurnal Cycle Climatology of Planetary Boundary Layer Height, *J. Climate*, 23, 5790–5809, <https://doi.org/10.1175/2010JCLI3552.1>, 2010.
- Lopez-Garcia, V., Neely III, R. R., Dahlke, S., and Brooks, I. M.: Low-level jets over the Arctic Ocean during MOSAiC, *Elementa*, 10, 00063, <https://doi.org/10.1525/elementa.2022.00063>, 2022.
- Marsik, F. J., Fischer, K. W., McDonald, T. D., and Samson, P. J.: Comparison of Methods for Estimating Mixing Height Used during the 1992 Atlanta Field Intensive, *J. Appl. Meteorol.*, 34, 1802–1814, [https://doi.org/10.1175/1520-0450\(1995\)034<1802:COMFEM>2.0.CO;2](https://doi.org/10.1175/1520-0450(1995)034<1802:COMFEM>2.0.CO;2), 1995.
- Maturilli, M., Holdridge, D. J., Dahlke, S., Graeser, J., Sommerfeld, A., Jaiser, R., Deckelmann, H., and Schulz, A.: Initial radiosonde data from 2019-10 to 2020-09 during project MOSAiC, Alfred Wegener Institute, Helmholtz Centre for Polar and Marine Research, Bremerhaven, PANGAEA [data set], <https://doi.org/10.1594/PANGAEA.928656>, 2021.
- Maturilli, M., Sommer, M., Holdridge, D. J., Dahlke, S., Graeser, J., Sommerfeld, A., Jaiser, R., Deckelmann, H., and Schulz, A.: MOSAiC radiosonde data (level 3), PANGAEA [data set], <https://doi.org/10.1594/PANGAEA.943870>, 2022.
- Nicolaus, M., Perovich, D., Spreen, G., Granskog, M., Albedyll, L., Angelopoulos, M., Anhaus, P., Arndt, S., Belter, H., Bessonov, V., Birnbaum, G., Brauchle, J., Calmer, R., Cardellach, E., Cheng, B., Clemens-Sewall, D., Dadic, R., Damm, E., de Boer, G., Demir, O., Dethloff, K., Divine, D., Fong, A., Fons, S., Frey, M., Fuchs, N., Gabarró, C., Gerland, S., Goessling, H., Gradinger, R., Haapala, J., Haas, C., Hamilton, J., Hannula, H.-R., Hendricks, S., Herber, A., Heuzé, C., Hoppmann, M., Høyland, K., Huntemann, M., Hutchings, J., Hwang, B., Itkin, P., Jacobi, H.-W., Jaggi, M., Jutila, A., Kaleschke, L., Katlein, C., Kolabutin, N., Krampe, D., Kristensen, S., Krumpfen, T., Kurtz, N., Lampert, A., Lange, B., Lei, R., Light, B., Linhardt, F., Liston, G., Loose, B., Macfarlane, A., Mahmud, M., Matero, I., Maus, S., Morgenstern, A., Naderpour, R., Nandan, V., Niubom, A., Oggieri, M., Oppelt, N., Pätzold, F., Perron, C., Petrovsky, T., Pirazzini, R., Polashenski, C., Rabe, B., Raphael, I., Regnery, J., Rex, M., Ricker, R., Riemann-Campe, K., Rinke, A., Rohde, J., Salganik, E., Scharien, R., Schiller, M., Schneebeli, M., Semmling, M., Shimanchuk, E., Shupe, M., Smith, M., Smolyanitsky, V., Sokolov, V., Stanton, T., Stroeve, J., Thielke, L., Timofeeva, A., Tonboe, R., Tavri, A., Tsamados, M., Wagner, D., Watkins, D., Webster, M., and Wendisch, M.: Overview of the MOSAiC expedition – Snow and sea ice, *Elementa*, 10, 000046, <https://doi.org/10.1525/elementa.2021.000046>, 2022.
- Nixdorf, U., Dethloff, K., Rex, M., Shupe, M., Sommerfeld, A., Perovich, D., Nicolaus, M., Heuzé, C., Rabe, B., Loose, B., Damm, E., Gradinger, R., Fong, A., Maslowski, W., Rinke, A., Kwok, R., Spreen, G., Wendisch, M., Herber, A., Hirsekorn, M., Mohaupt, V., Frickenhaus, S., Immerz, A., Weiss-Tuider, K., König, B., Mengedoht, D., Regnery, J., Gerchow, P., Ransby, D., Krumpfen, T., Morgenstern, A., Haas, C., Kanzow, T., Rack, F. R., Saitzev, V., Sokolov, V., Makarov, A., Schwarze, S., Wunderlich, T., Wurr, K., and Boetius, A.: MOSAiC Extended Acknowledgement, Zenodo, <https://doi.org/10.5281/zenodo.5179738>, 2021.
- NOAA's Global Ocean Monitoring and Observing Program: <https://doi.org/10.13039/100018302>, 2021.
- Rabe, B., Heuzé, C., Regnery, J., Aksenov, Y., Allerholt, J., Athanase, M., Bai, Y., Basque, C., Bauch, D., Baumann, T. M., Chen, D., Cole, S. T., Craw, L., Davies, A., Damm, E., Dethloff, K., Divine, D. V., Doglioni, F., Ebert, F., Fang, Y.-C., Fer, I., Fong, A. A., Gradinger, R., Granskog, M. A., Graupner, R., Haas, C., He, H., He, Y., Hoppmann, M., Janut, M., Kadko, D., Kanzow, T., Karam, S., Kawaguchi, Y., Koenig, Z., Kong, B., Krishfield, R. A., Krumpfen, T., Kuhlmeier, D., Kuznetsov, I., Lan, M., Laukert, G., Lei, R., Li, T., Torres-Valdés, S., Lin, L., Lin, L., Liu, H., Liu, N., Loose, B., Ma, X., McKay, R., Mallet, M., Mallett, R. D. C., Maslowski, W., Mertens, C., Mohrholz, V., Muilwijk, M., Nicolaus, M., O'Brien, J. K., Perovich, D., Ren, J., Rex, M., Ribeiro, N., Annette, A., Schaffer, J., Schuffenhauer,

- I., Schulz, K., Shupe, M. D., Shaw, W., Sokolov, V., Sommerfeld, A., Spreen, G., Stanton, T., Stephens, M., Su, J., Sukhikh, N., Sundfjord, A., Thomisch, K., Tippenhauer, S., Toole, J. M., Vredenburg, M., Walter, M., Wang, H., Wang, L., Wang, Y., Wendisch, M., Zhao, J., Zhou, M., and Zhu, J.: Overview of the MOSAiC expedition: Physical oceanography, *Elementa*, 10, 00062, <https://doi.org/10.1525/elementa.2021.00062>, 2022.
- Rantanen, M., Karpechko, A. Y., Lipponen, A., Nordling, K., Hyvärinen, O., Ruosteenoja, K., Vihma, T., and Laarksonen, A.: The Arctic has warmed nearly four times faster than the globe since 1979, *Commun. Earth Env.*, 3, 168, <https://doi.org/10.1038/s43247-022-00498-3>, 2022.
- Schmithüsen, H. and Raeke, A.: Meteorological observations during POLARSTERN cruise PS122/1, Alfred Wegener Institute, Helmholtz Centre for Polar and Marine Research, Bremerhaven, PANGAEA [data set], <https://doi.org/10.1594/PANGAEA.935263>, 2021a.
- Schmithüsen, H., and Raeke, A.: Meteorological observations during POLARSTERN cruise PS122/4, Alfred Wegener Institute, Helmholtz Centre for Polar and Marine Research, Bremerhaven, PANGAEA [data set], <https://doi.org/10.1594/PANGAEA.935266>, 2021b.
- Schmithüsen, H., and Raeke, A.: Meteorological observations during POLARSTERN cruise PS122/5, Alfred Wegener Institute, Helmholtz Centre for Polar and Marine Research, Bremerhaven, PANGAEA [data set], <https://doi.org/10.1594/PANGAEA.935267>, 2021c.
- Seibert, P., Beyrich, F., Gryning, S. E., Joffre, S., Rasmussen, A., and Tercier, P.: Review and Intercomparison of Operational Methods for the Determination of the Mixing Height, *Atmos. Environ.*, 34, 1001–102, [https://doi.org/10.1016/S1474-8177\(02\)80023-7](https://doi.org/10.1016/S1474-8177(02)80023-7), 2000.
- Serreze, M. and Barry, R.: Processes and impacts of Arctic amplification: A research synthesis, *Global Planet. Change*, 77, 85–96, <https://doi.org/10.1016/j.gloplacha.2011.03.004>, 2011.
- Serreze, M. and Franics, J.: The Arctic amplification debate, *Climatic Change*, 76, 241–246, <https://doi.org/10.1007/s10584-005-9017-y>, 2006.
- Shupe, M. D., Rex, M., Dethloff, K., Damm, E., Fong, A. A., Gradinger, R., Heuzé, Loose, C., B., Makarov, A., Maslowski, W., Nicolaus, M., Perovich, D., Rabe, B., Rinke, A., Sokolov, V., and Sommerfeld, A.: The MOSAiC Expedition: A Year Drifting with the Arctic, NOAA Arctic Report Card, 1–8, <https://doi.org/10.25923/9g3v-xh92>, 2020.
- Shupe, M., Chu, D., Costa, D., Cox, C., Creamean, J., de Boer, G., Dethloff, K., Engelmann, R., Gallagher, M., Hunke, E., Maslowski, W., McComiskey, A., Osborn, J., Persson, O., Powers, H., Pratt, K., Randall, D., Solomon, A., Tjernström, M., Turner, D., Uin, J., Uttal, T., Verlinde, J., and Wagner, D.: Multidisciplinary drifting Observatory for the study of Arctic Climate (MOSAIC) Field Campaign Report, ARM user facility, DOE/SC-ARM-21-007, <https://doi.org/10.2172/1787856>, 2021.
- Shupe, M. D., Rex, M., Blomquist, B., Persson, P. O. G., Schmale, J., Uttal, T., Althausen, D., Angot, H., Archer, S., Bariteau, L., Beck, I., Bilberry, J., Bucci, S., Buck, C., Boyer, M., Brasseur, Z., Brooks, I. M., Calmer, R., Cassano, J., Castro, V., Chu, D., Costa, D., Cox, C. J., Creamean, J., Crewell, S., Dahlke, S., Damm, E., de Boer, G., Deckelmann, H., Dethloff, K., Dütsch, M., Ebell, K., Ehrlich, A., Ellis, J., Engelmann, R., Fong, A. A., Frey, M. M., Gallagher, M. R., Ganzeveld, L., Gradinger, R., Graeser, J., Greenamyre, V., Griesche, H., Griffiths, S., Hamilton, J., Heinemann, G., Helmig, D., Herber, A., Heuzé, C., Hofer, J., Houchens, T., Howard, D., Inoue, J., Jacobi, H.-W., Jaiser, R., Jokinen, T., Jourdan, O., Jozef, G., King, W., Kirchgaessner, A., Klingebiel, M., Krassovski, M., Krumpfen, T., Lampert, A., Landing, W., Laurila, T., Lawrence, D., Lonardi, M., Loose, B., Lüpkes, C., Maahn, M., Macke, A., Maslowski, W., Marsay, C., Maturilli, M., Mech, M., Morris, S., Moser, M., Nicolaus, M., Ortega, P., Osborn, J., Pätzold, F., Perovich, D. K., Petäjä, T., Pilz, C., Pirazzini, R., Posman, K., Powers, H., Pratt, K. A., Preußer, A., Quélever, L., Radenz, M., Rabe, B., Rinke, A., Sachs, T., Schulz, A., Siebert, H., Silva, T., Solomon, A., Sommerfeld, A., Spreen, G., Stephens, M., Stohl, A., Svensson, G., Uin, J., Viégas, J., Voigt, C., von der Gathen, P., Wehner, B., Welker, J. M., Wendisch, M., Werner, M., Xie, Z. Q., and Yue, F.: Overview of the MOSAiC expedition: Atmosphere, *Elementa*, 10, 00060, <https://doi.org/10.1525/elementa.2021.00060>, 2022.
- Silva, T. and Schlosser, E.: A 25-year climatology of low-tropospheric temperature and humidity inversions for contrasting synoptic regimes at Neumayer Station, Antarctica, *Weather Clim. Dynam. Discuss.* [preprint], <https://doi.org/10.5194/wcd-2021-22>, 2021.
- Sivaraman, C., McFarlane, S., Chapman, E., Jensen, M., Toto, T., Liu, S., and Fischer, M.: Planetary Boundary Layer (PBL) Height Value Added Product (VAP): Radiosonde Retrievals. ARM User Facility, DOE/SC-ARM/TR-132, 2013.
- Stroeve, J. C., Kattsov, V., Barrett, A., Serreze, M., Pavlova, T., Holland, M., and Meier, W. N.: Trends in Arctic Sea Ice Extent from CMIP5, CMIP3 and Observations, *Geophys. Res. Lett.*, 39, 1–7, <https://doi.org/10.1029/2012GL052676>, 2012.
- Stull, R. B.: An Introduction to Boundary Layer Meteorology, Kluwer Academic Publishers, the Netherlands, 670 pp., <https://doi.org/10.1007/978-94-009-3027-8>, 1988.
- Tjernström, M. and Graversen, R. G.: The vertical structure of the lower Arctic troposphere analysed from observations and the ERA-40 reanalysis, *Q. J. Roy. Meteor. Soc.*, 135, 431–443, <https://doi.org/10.1002/qj.380>, 2009.
- Tjernström, M., Leck, C., Persson, P. O. G., Jensen, M. L., Onclay, S. P., and Targino, A.: The Summertime Arctic Atmosphere: Meteorological Measurements during the Arctic Ocean Experiment 2001, *B. Am. Meteorol. Soc.*, 85, 1305–1321, <https://doi.org/10.1175/BAMS-85-9-1305>, 2004.
- Tjernström, M., Birch, C. E., Brooks, I. M., Shupe, M. D., Persson, P. O. G., Sedlar, J., Mauritsen, T., Leck, C., Paatero, J., Szczodrak, M., and Wheeler, C. R.: Meteorological conditions in the central Arctic summer during the Arctic Summer Cloud Ocean Study (ASCOS), *Atmos. Chem. Phys.*, 12, 6863–6889, <https://doi.org/10.5194/acp-12-6863-2012>, 2012.
- Tuononen, M., Sinclair, V. A., and Vihma, T.: A climatology of low-level jets in the mid-latitudes and polar regions of the Northern Hemisphere, *Atmos. Sci. Lett.*, 16, 492–499, <https://doi.org/10.1002/asl.587>, 2015.
- Winton, M.: Amplified Arctic climate change: What does surface albedo feedback have to do with it?, *Geophys. Res. Lett.*, 33, L03701, <https://doi.org/10.1029/2005GL025244>, 2006.